KOM
CORROSION AND MATERIAL PROTECTION JOURNAL

ORIGINAL ARTICLE

ASSOCIATION OF CZECH AND SLOVAK CORROSION ENGINEERS

Characterization of nickel (II) oxide nanoparticles synthesized by chemical precipitation technique for corrosion inhibition applications

Kooffreh Okon[1,2], Christogonus Oudney Akalezi[1], Taofik Oladimeji Azeez[1], Ikechukwu Ignatius Ayogu[1]

[1] Africa Centre of Excellence in Future Energies and Electrochemical Systems, Federal University of Technology, PMB 1526 Owerri (ACE-FUELS, FUTO), Imo State, Nigeria.

[2] Department of Materials and Metallurgical Engineering, Federal University of Technology, PMB 1526 Owerri, Imo State, Nigeria

E-mail: koofsco1@gmail.com

A novel approach for synthesizing nickel (II) oxide (NiO) nanoparticles was developed by chemically precipitating nickel (II) chloride ($NiCl_2$) derived from dissolving pure solid nickel in concentrated hydrochloric acid. The synthesized nanoparticles were then characterized and evaluated as a corrosion inhibitor for mild steel. Structural, morphological, and thermal properties were analyzed using XRD, FTIR, TEM, SEM-EDX, TGA/DTA, and DSC techniques. The nanoparticles exhibited a highly crystalline structure with an average crystallite size of 23.03 nm, which was consistent with TEM analysis showing individual particle sizes between 10.02 and 28.50 nm. Thermal analysis revealed a significant decomposition event at 519.4 °C, indicating high thermal stability. The corrosion inhibition potential was assessed on mild steel specimens coated with an epoxy resin containing 1 wt. % NiO nanoparticles and immersed in a 3.5 wt. % NaCl solution. The results demonstrated a substantial decrease in corrosion rate with the addition of NiO. The epoxy-1 wt% NiO nanocomposite coating provided the highest inhibition efficiency compared to the sample coated with only epoxy resin and the uncoated sample reaching 91.0 % and required a higher activation energy to initiate corrosion compared to both uncoated and neat epoxy-coated samples. This study confirms the successful synthesis of stable, crystalline NiO nanoparticles via a novel chemical precipitation method and establishes their superior performance as an active component in epoxy coatings for robust corrosion protection of mild steel.

INTRODUCTION

Metal oxides are of great technological relevance in photovoltaic applications, clean energy production, sensors, biological uses, nanoelectronics devices, solar cells, catalysis, corrosion protection and environmental remediation due to their unique arrangement of electronic structure, light absorption properties, unique catalytic capability, plasmonic tunability, relatively low toxicity and charge transport characteristics [1–3]. Nanoparticles (NPs) of metal oxides are preferred to their bulk counterparts due to their enormous surface area to volume ratio [4]. Al_2O_3, ZrO_2, TiO_2, Y_2O_3, NiO, ZnO and SnO_2 are the most frequently used metal oxide nanoparticles [5]. NiO nanoparticles are of spe-cial interest due to their unique combination of high hardness [6], excellent thermal stability [7], electronic [8], catalytic [9], magnetic[10] and optical properties [11]. Diverse methods including precipitation [12], sol-gel [13], solvothermal [14], sonochemistry [15], thermal decomposition [16], microwaves [17], pulse-laser ablation [18], anodic arc plasma [19] and green synthesis [20] have been used to synthesize metal oxide nanoparticles particularly nickel (II) oxide nanoparticles. Rifaya et. al synthesized spherical and rod-shaped polycrystalline nickel (II) oxide nanoparticles with average particle size of 12 nm, specific surface area of 74 m^2g^{-1} and energy band gap of 3.83 eV by chemical capping method using nickel chloride, alanine, ethanol and ammonia. Solution A consisting of 0.1 M solution of $NiCl_3$ in ethanol was added drop wise to solution B consisting of 0.001 M solution of alanine in ammonia with continuous stirring at a temperature of 80 °C for 20 hrs. The nanoparticles were collected and washed several times in high purity water to remove the excess ions. The samples were dried at 60 °C in air to remove moisture contents. The samples were prepared by heating this $Ni(OH)_3$ nanoparticles at 350 °C for 90 min [21]. Salavati-niasari et al. synthe-sized quasi-spherical nickel and nickel (II) oxide nanoparticles with average particle size of 24 nm having magnetic coercivity of Ni nanoparticles as high as 900 A/m via nontoxic, facile and inexpensive heat-treatment of nickel octanoate precursor in the range of 400-900 °C. The optical absorption band gap of the synthesized NiO nanoparticles was reported to be 3.41 eV [22]. Danial et al. synthesized nickel (II) oxide nanoparticles by sol-gel technique by heating a mixture of nickel nitrate precursor (Ni

$(NO_3)_2.6H_2O$) solution dripped in citric acid ($C_6H_8O_7.H_2O$) solution to 70 °C with mechanical stirring for about 12 h dripping followed by aging and drying of the obtained translucent green gel at 110 °C for 24 h and subsequent calcination at three different temperatures of 200 °C, 400 °C and 600 °C for 4 h. Average particle sizes of 10 nm, 20 nm and 42 nm were obtained for calcination temperatures of 200 °C, 400 °C and 600 °C respectively [23]. Hada et al. synthesized nanoparticles of nickel (II) oxide with average particle size of 14 nm with pure bunsenite phase and FCC crystal structure with spherical morphology through a mixed reverse microemulsion route. The microemulsion was prepared by Tween-80, Aerosol-OT, n-Propanol, Cyclohexane, and Nickel Chloride. Liquid ammonia solution was added dropwise to the microemulsion mixture to using a magnetic stirrer at room temperature form precipitate of nickel (II) hydroxide which was subsequently filtered and washed repeatedly to remove organic residues and surfactant. This was followed by drying in an air oven at 80 °C for 10 h and calcination at 450 C for 3 h in muffle furnace [24]. Nathan et al. synthesized crystalline nanostructured nickel (II) oxide with particle size within 7–15 nm range having a single phase for electrochemical capacitors via the solvothermal synthesis route using nitrate–citrate precursor having $Ni(NO_3)_2$ as starting material. The thermal decomposition of the as-formed gel precursor led to the formation of crystalline NiO [25]. Ortega et al. synthesized spherical and hexagonal ferromagnetic nickel and nickel (II) oxide nanoparticles with particle sizes ranging from 11.2 nm to 87 nm by a levitation-jet aerosol synthesis under different gas environments and metal precursor feed rates [26]. Sheit et al. synthesized cubic cluster-like structure NiO nanoparticle powder by adding 0.1 molar nickel nitrate hexahydrate ($Ni(NO_3)_2{\cdot}6H_2O$) to *Acacia Nilotica* bark extract and the mixture was stirred continuously for 6 hours at a steady temperature of 80.0 °C to obtain a black precipitate which was dried at 120 °C for 6 hours and subsequently calcined at 500 °C for 5 h [27]. Firisa et al. carried out green synthesis of NiO NPs with average particle size of 14.18 nm by adding Phytolacca dodecandra L'Herit Leaf extract to nickel(II) nitrate hexahydrate ($Ni(NO_3)_2{\cdot}6H_2O$) with pH adjustment to 10 using 5M NaOH. The obtained precipitate was centrifuged for 10 min, washed with distilled water and ethanol several times to remove impurities, dried at 70 °C for 2 h in an oven and calcined in a muffle furnace for 2 h at 400 °C [28]. In this work, the nickel (II) chloride ($NiCl_2$) precursor which was reacted with sodium hydroxide (NaOH) to form nickel (II) hydroxide [$Ni(OH)_2$] precipitate which was further calcined to obtain NiO nanoparticles was obtained by dissolving pure solid nickel in concentrated Hydrochloric acid. Structural, morphological, compositional and thermal analysis of the synthesized samples were carried out using a combination of XRD, FTIR, TEM, SEM-EDX, TGA/DTA and DSC techniques. The relentless degradation of materials due to corrosion presents a critical challenge across global industries, incurring significant economic costs and compromising the integrity of essential infrastructure [29]. With annual damage estimates exceeding 2.5 trillion U.S dollars, a substantial portion of this loss is directly attributed to the corrosion of steel components. While traditional strategies such as organic coatings and cathodic protection have been employed, many conventional organic corrosion inhibitors are environmentally hazardous and offer limited long-term protection [30–35]. This dual challenge of economic impact and environmental unsustainability necessitates the urgent development of a new generation of high-performance, eco-friendly materials for corrosion prevention.

Nanotechnology offers a transformative solution to this problem, leveraging the unique properties of nanoparticles to create highly effective corrosion inhibitors. Nanoparticles, particularly metal oxides, are ideal for this application due to their high surface area-to-volume ratio, which promotes the formation of a dense, passive barrier on metal surfaces [36]. Among these materials, nickel (II) oxide (NiO) nanoparticles are particularly promising, exhibiting excellent chemical stability and low toxicity [37]. While the potential of NiO nanoparticles is widely recognized, existing synthesis methods often rely on complex, energy-intensive processes or expensive precursors. This limitation has impeded their large-scale, cost-effective production and broader industrial application.

The potential of using the synthesized NiO nanoparticles as corrosion inhibitor was evaluated by studying the corrosion resistance of mild steel (MS) coated with epoxy resin containing 1 wt. % NiO in 3.5 wt. % NaCl within the temperature range of 30 to 60 °C using gravimetric method.

MATERIALS AND METHODS

Synthesis and characterization of synthesized NiO nanoparticles

The nickel (II) oxide nanoparticles were synthesized by the chemical precipitation technique. The synthesis procedure for the nickel (II) oxide nanoparticles have been described in details in our previously reported work [38].

XRD characterization to determine the crystal structure, average crystallite size and lattice parameter of the synthesized nickel (II) oxide nanoparticles sample was done using Thermo Scientific ARL X'TRA X-ray Diffractometer with serial number 197492086, a product of Thermo fisher Scientific Company Switzerland. The equipment has an X-ray tube operating at 60 kV, 2200 Wt

(MC 61-04x 12C, Ni-filter) and generator voltage of 10-60 kV and current strength of 0-50 $_M$A. Cu was used as the target, and the corresponding wavelength of the X-ray was 0.154056 nm. The FTIR characterization to detect the presence of possible functional groups and chemical bonds in the synthesized nickel (II) oxide nanoparticles sample was done using the PerkinElmer Instrument, Spectrum Two FT-IR Spectrometer ($LiTaO_3$ Detector) with serial number 122344. Four scans were performed within the range of 4000 to 450 cm^{-1}. A Fourier Transform Infrared Spectrophotometer (FTIR) is an analytical instrument used to measure the absorption or transmission of infrared radiation by a sample. The FTIR technique is based on the principle that different chemical bonds in a molecule absorb infrared radiation at specific frequencies, and by measuring the absorption or transmission of this radiation, it is possible to identify the types of chemical bonds present in the sample. TGA/DTA characterization of 8.312 mg nickel (II) oxide nanoparticles sample within the heating range of 30 °C to 950 °C at the scanning rate of 10 °C/min was done using the PerkinElmer TGA 4000 equipment made in the Netherlands to determine the thermal stability of the synthesized sample by recording continuous measurements of mass as a function of temperature. DSC characterization of 7.5000 mg of Nickel oxide nanoparticles sample at a heating rate of 10 °C/min was done using the Differential Scanning Calorimeter (DSC) Model Mettler Toledo DSC 2. The DSC measures heat flow associated with thermal transitions of a material such as glass transition, melting point and crystallization temperature. AFM characterization of Nickel (II) oxide nanoparticles sample to obtain nanoscale imaging of topographical morphology and surface roughness of the sample was done using the nGauge Atomic Force Microscope manufactured by ICSPI, Canada with Maximum scan area (XY) of 20 × 20 µm, Z range of 10 µm, scan speed of 80 seconds (256 × 256 pixel, of 20 × 20 µm), noise floor <0.5 nm rms and XY scanner resolution of <0.5 nm. The morphology of the synthesized nickel oxide nanoparticles was studied using the JEOL JSM 7600F Scanning Electron Microscope at three different magnifications of 8000×, 9000× and 10 000× respectively at Hv of 20 KV. The size of individual particles of the synthesized nickel (II) oxide nanoparticles was recorded using the JEM-ARM200F-G model of the Transmission Electron Microscope.

Corrosion testing

The coatings were prepared using the method adopted by Khodair et al. [39] with slight modification. The coatings for the mild steel specimens were produced by mixing epoxy resin based on diglycidyl ether of bisphenol A (DGEBA) with an amine hardener, tetraethylenepentamine (TEPA) in the ratio of 2:1 by weight. 1 wt. % NiO were added to the coating mixture and the contents were mechanically stirred for about 30 minutes and ultrasonicated for about 15 minutes for homogenization. Well cleaned mild steel specimens suspended by polymeric threads were fully dipped into the coating mixture and subsequently dried at room temperature for 48 hours for full curing. The corrosion inhibition data for mild steel in the presence and absence of epoxy-NiO nanoparticles for 60 days of immersion in 3.5 wt. % NaCl was obtained using the gravimetric method. Corrosion rate and percentage inhibition efficiency were calculated using the formulae in equations 1 and 2 respectively.

$$CR = \frac{W}{At} \tag{1}$$

where CR is the Corrosion rate (gm^{-2} day^{-1}), A is the surface Area (m^2) and t is the exposure time (days). The corrosion inhibition efficiency was calculated using the formula:

$$\text{I.E.} = \frac{CR^0 - CR^i}{CR^0} \cdot 100\ \% \tag{2}$$

where I.E. is percentage inhibition efficiency, CR^0 is corrosion rate of uncoated sample, and CR^i is corrosion rate of coated sample.

Surface studies

The surface of the blank sample and samples coated with the pristine epoxy resin as well as epoxy resin containing 1 wt. % NiO nanoparticles were studied after 60 days immersion in 3.5 wt. % NaCl using the nGauge Atomic Force Microscope with Maximum scan area (XY) of 20 × 20 µm, Z range of 10 µm, scan speed of 80 seconds (256 × 256 pixel, of 20 × 20 µm), noise floor <0.5 nm rms and XY scanner resolution of <0.5 nm to obtain the surface roughness of the various samples.

RESULTS AND DISCUSSION

Structural analysis

X-ray diffraction (XRD) is a nondestructive technique for characterizing crystalline materials [40]. It gives information regarding the structures, phases, crystal structure, lattice parameters, chemical composition and other structural parameters, such as average grain size, crystallinity, strain, and crystal defects [41, 42]. X-ray diffraction peaks are produced by constructive interference of a monochromatic beam of X-rays scattered at specific angles from each set of lattice planes in a sample. The peak intensities are determined by the distribution of atoms within the lattice [43]. The XRD pattern for the synthesized nickel (II) oxide nanopartic-les is shown in Figure 1. The X-ray diffraction data (Tab. 1)

showed distinct diffraction peaks identified at 2θ values of 37.25°, 43.27°, 56.62° and 63.05° representing cubic crystallites of NiO corresponding to the diffracting planes (111), (200), (222) and (220) respectively with a lattice constant of 4.1749 (DB Card number 01-076-6122). The other peaks observed at diffraction angles of 31.87° and 45.61° have been identified as Ni_2O_3 and Ni and correspond to the (200) and (220) diffracting planes [44].

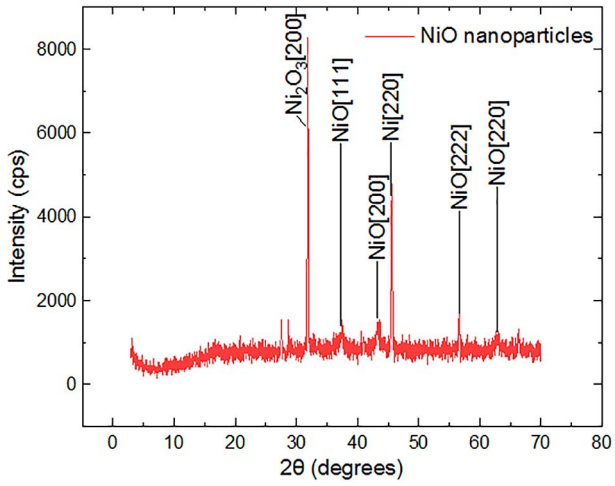

Fig. 1. XRD pattern of synthesized NiO nanoparticles

The broadened peak shows the nanometer-sized crystallites. The average crystallite size, D was calculated by using the Debye-Scherrer formula [45] which is given as

$$D = \frac{\text{Shape factor} \times \text{x-ray wavelength}}{\text{Full width at half maximum, FWMH} \times \cos\Theta} \quad (3)$$

The crystallite sizes were found to be within the range of 9.9 nm and 53.8 nm for various identified diffraction peaks (Tab. 1) resulting in an average crystallite size of 23.03 nm which is consistent with the individual particle sizes ranging from 10.02 nm to 28.50 nm for NiO nanoparticles revealed by Transmission Electron Microscopy results as illustrated by figure 2. The TEM image shows that the NiO particles are predominantly spherical or near-spherical in shape. Their surfaces appear relatively smooth. The image shows several diameters of individual particles. The measured sizes range from 10.02 nm to 28.50 nm. This confirms that the material consists of nanoparticles, with a size distribution that is relatively narrow, centered around a certain average size likely in the mid-to-high tens of nanometers.

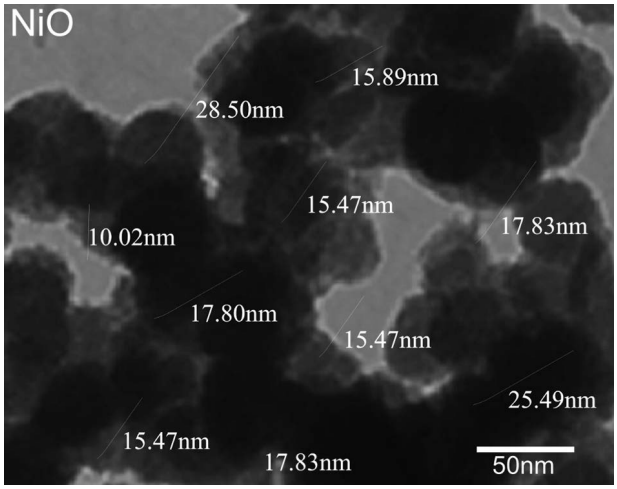

Fig. 2. TEM analysis of synthesized nickel (II) oxide nanoparticles

The Fourier Transform Infrared Spectroscopy (FTIR) analysis of the synthesized nickel (II) oxide nanoparticles shown in Figure 3 revealed that some characteristic infrared absorption peaks including nickel-oxygen tetrahedral bonding, metal-oxygen stretching and oxygen-hydrogen bonding were present in the synthesized sample. Metal-oxygen stretching was confirmed at wavenumber of 579 cm^{-1} which is typically observed for NiO with a strong peak around 500-600 cm^{-1} [19]. Nickel-oxygen tetrahedral bonding was noticed at 944 cm^{-1} which is another peak associated with Ni–O bonding, but typically at slightly higher wavenumbers for NiO, around 684-964 cm^{-1} and represents the distinctive mode of the NiO phase [20]. The presence of oxygen-hydrogen bonding was strongly confirmed by two prominent peaks at 1624 and 3350 cm^{-1} due to the hydroxyl groups present at the surface of the sample. Metal oxides can interact with moisture and atmospheric

Tab. 1 XRD data of synthesized NiO nanoparticles

Diffraction angle (2θ)	d-value (Å)	FWHM (°)	Height (cps)	Diffracting plane	Crystallite size (nm)
31.871(8)	2.8056(7)	0.164(6)	5525(251)	(200)	52.7(20)
37.25(5)	2.412(3)	0.88(15)	209(27)	(111)	9.9(16)
43.27(11)	2.089(5)	0.68(12)	367(42)	(200)	13.2(24)
45.606(10)	1.9876(4)	0.183(10)	3010(193)	(220)	49.1(26)
56.62(2)	1.6242(6)	0.18(3)	727(66)	(222)	53.8(80)
63.05(4)	1.4733(8)	0.64(16)	209(25)	(220)	15.2(38)

gases leading to the formation of hydroxyl groups on the surface. Peaks associated with hydroxyl stretching and bending vibrations are typically observed in the range 3000-3700 cm^{-1} and 1600-1800 cm^{-1} respectively [46, 47].

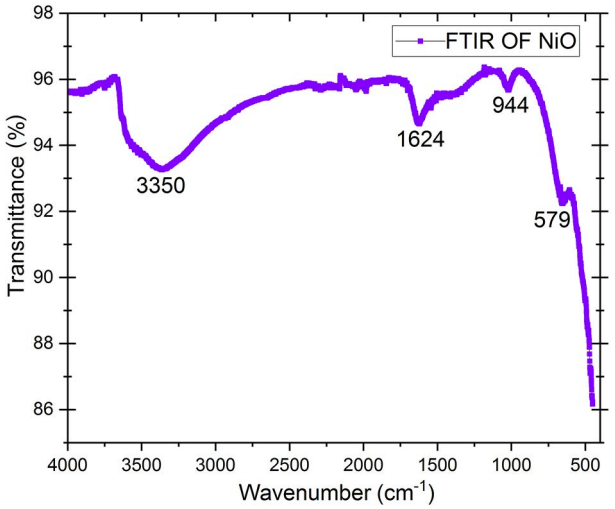

Fig. 3. FTIR spectrum for the synthesized Nickel (II) oxide nanoparticles

Morphological and compositional analyses of the synthesized nickel (II) oxide nanoparticles

The morphology of the synthesized nickel (II) oxide nanoparticles investigated using the JEOL JSM 7600F Scanning Electron Microscope captured at three different magnifications of 8000×, 9000× and 10 000× is shown in Figures 4, 5 and 6 respectively.

The SEM micrographs reveal a microscopic structure characterized by irregular, tightly packed particles and agglomeration of several nanoparticles of nickel (II) oxide to form clusters, resulting in a porous and non-uniform surface morphology. This type of structure can have significant implications for the material's properties, particularly its high surface area, which is a desirable trait for applications like catalysis, gas sensing and corrosion inhibition. The irregular shapes and varied sizes of the NiO particles create a tortuous path for corrosive agents (like chloride ions and water) to penetrate the coating. This tortuosity effect increases the diffusion length, slowing down the attack on the steel substrate.

The EDX results for the compositional analysis for the synthesized nickel (II) oxide nanoparticles is shown in Figure 7.

It can be seen clearly from the EDX pattern above that the composition of the synthesized nickel (II) oxide nanoparticles has a major composition of 67.9 % Ni. A small portion of other trace elements such as Cu, Zr, Fe, S and K were also present with composition of 4.7 % Cu, 4.1 % Zr, 3.7 % Fe, 2.6 % S and 3.2 % K respectively. The Quantitative information about the

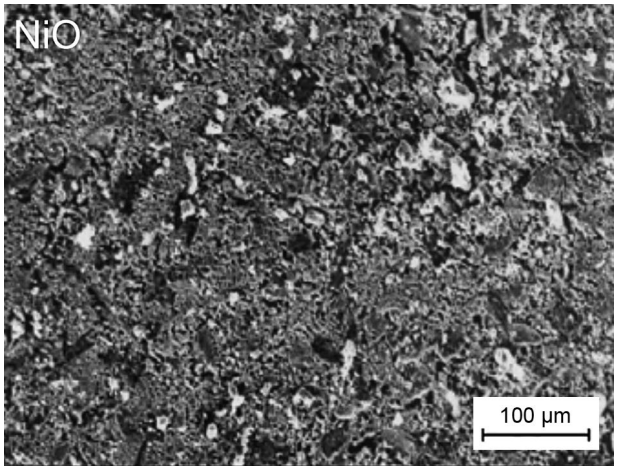

Fig. 4. SEM micrograph showing clusters of nickel (II) oxide nanoparticles (8000x)

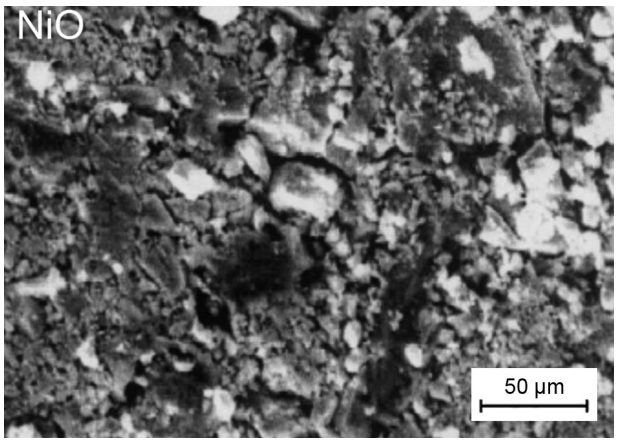

Fig. 5. SEM micrograph indicating clusters of nickel (II) oxide nanoparticles (9000x)

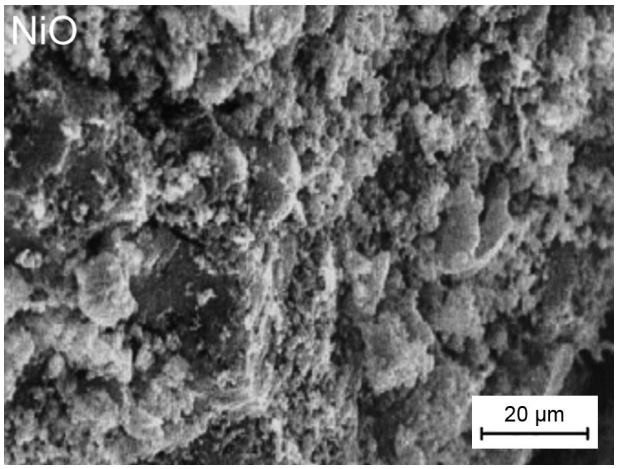

Fig. 6. SEM micrograph depicting clusters of nickel (II) oxide nanoparticles (10 000x)

morphology and surface roughness of the synthesized Nickel (II) oxide nanoparticles were studied using Atomic Force Microscopy (AFM) and the micrograph obtained is illustrated in Figure 8.

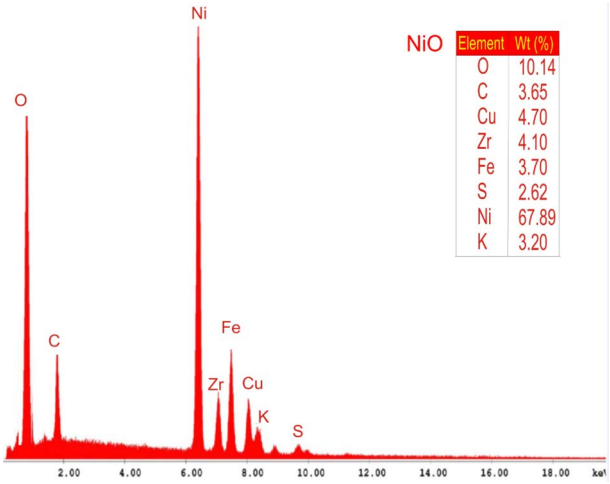

Fig. 7. EDX pattern of synthesized nickel (II) oxide nanoparticles

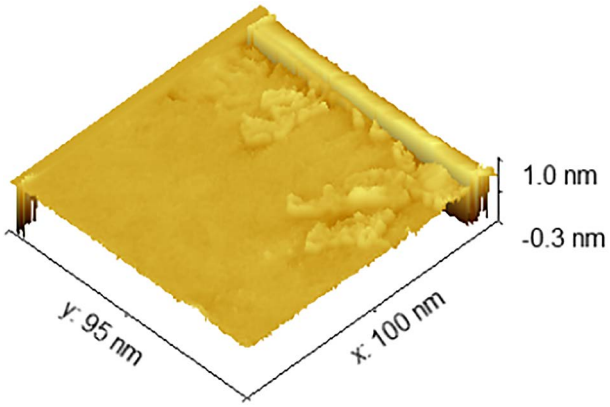

Fig. 8. AFM micrograph for the synthesized Nickel (II) oxide nanoparticles

AFM data revealed that the micrograph contains 611 grains with a density of 64575.4 µm² and a total projected area (abs.) of 8828.80 nm² while the total projected area (rel.) was 93.31 %. The mean grain area recorded was 14.45 nm² while the Mean grain size was 1.91149 nm. An average roughness value of 0.728 nm was obtained while the values of 78.847 nm and 41.737 nm were recorded for RMS roughness (S_q) and Mean roughness (S_a) respectively. The Maximum peak height (S_p), Maximum pit depth (S_v) and Maximum height (S_z) obtained were 0.290 nm, 0.998 nm and 1.288 nm respectively. The AFM image confirms that the NiO sample has a non-uniform, granular surface at the nanoscale, with small height variations. This surface roughness is an important property that can influence the material's performance in applications where surface area and interaction with other materials are critical. The AFM results are consistent with the findings from SEM and TEM, which also showed a particulate and granular morphology.

Thermal analysis of the synthesized nickel (II) oxide nanoparticles

Thermal analysis techniques are essential for a wide range of materials such as polymers, composites, pharmaceutical products, food packaging, fuels, energy, chemicals, and many more [48–50]. These techniques, such as thermogravimetric analysis (TGA) and differential scanning calorimetry (DSC), usually measure heat transfer, weight loss, difference in size, or mechanical properties, as a function of change in temperature [51, 52]. The thermogravimetric analysis (TGA) or derivative thermogravimetry (DTG) is an important laboratory tool used for the characterization of composite material. It measures the mass of material as temperature changes over time [53]. The TGA/DTA technique was performed within the temperature range of 0 to 880 °C to provide insight into mass changes of synthesized nickel (II) oxide nanoparticles. The TGA, DTA and combined TGA/DTA and DSC analyses for the synthesized Nickel (II) oxide nanoparticles are shown in Figures 9-11 respectively. The TGA curve shows three distinct weight loss regions with the first region occurring between 0 to 300.9 °C and indicating a minimal weight loss of about 9.6 % suggesting that the sample is stable and no significant decomposition or phase transitions occur in this temperature range. This minimal weight loss can be attributed to the loss of moisture, volatile components and hydroxyl groups that attached to the surface of the metal oxide during synthesis. The second region occurring between 300.9 °C and 552.1 °C suggests significant thermal decomposition and possibly the loss of volatile components. A very significant weight loss of about 82.5 % took place within this phase due to thermal decomposition events. For nickel (II) oxide, it indicates the reduction of NiO to Ni and the removal of any residual solvent or moisture from synthesis.

The third region of the TGA graph occurring between 552.1 °C and 880 °C indicates thermal stability with no significant thermal events occurring in this range due to the completion of primary thermal decomposition processes within the second region of the curve. This means that the sample has reached a stable state with no further significant weight loss.

The portion of the DTA curve within the range of 0 °C to 240.2 °C indicates thermal stability similar to the portion of the TGA curve between 0 °C to 300.9 °C with no significant thermal events occurring in this range except evaporation of moisture, some volatile components and surface hydroxyl groups. The sharp endothermic peak observed at 480.8 °C indicates a very specific thermal event such as phase transition or a decomposition reaction occurring at this temperature, likely related to the structural changes of nickel (II) oxide or its stability.

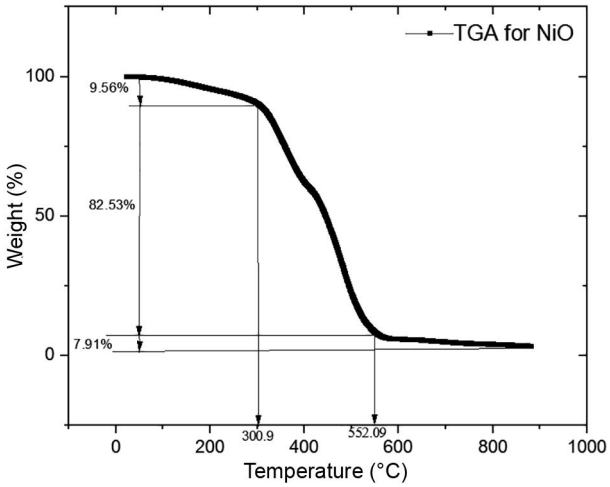

Fig. 9. TGA analysis for synthesized Nickel (II) oxide nanoparticles

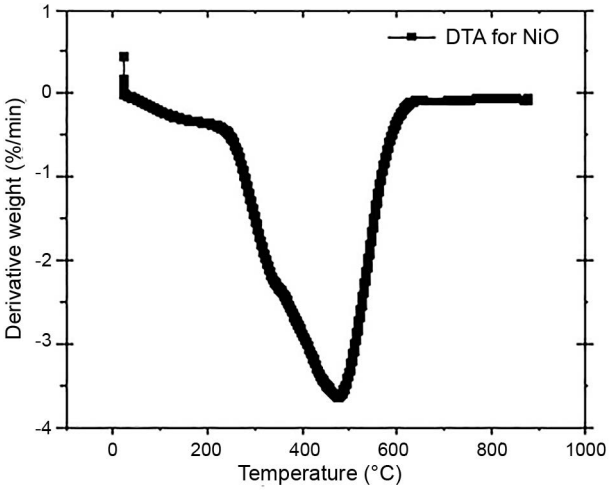

Fig. 10. DTA analysis for the synthesized Nickel (II) oxide nanoparticles

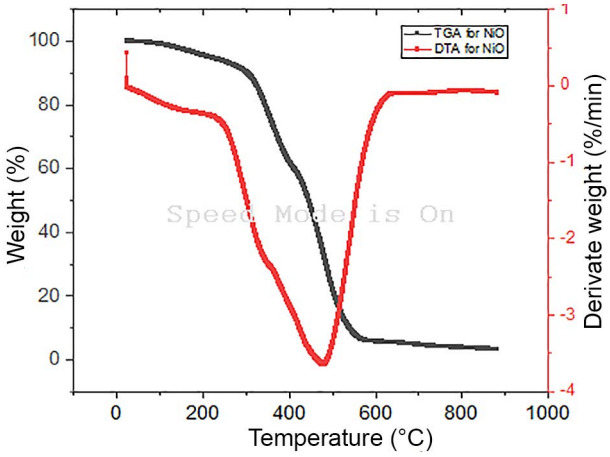

Fig. 11. TGA/DTA Analysis for the synthesized Nickel (II) oxide nanoparticles

The positive slope of the DTA curve observed between at 480.8 °C and at 637.6 °C after the endothermic peak indicates that the sample was still undergoing further decomposition or additional reactions that consume energy potentially indicating further loss of mass or structural transformation. The portion of the DTA curve noticed between 637.6 °C and 880.0 °C indicates stability at higher temperatures suggesting completion of thermal reactions or decomposition consistent with the TGA result in the same temperature range. The point of intersection of the TGA and DTA for the synthesized nickel (II) oxide nanoparticles occurring at a temperature of 519.4 °C corresponding to a weight loss of about 90 % represents the critical point where significant thermal changes (decomposition or phase transitions) occur. It serves as a benchmark of thermal stability for the sample [54]thereby obtaining multiaspect thermal information of the material such as dehydration, structural decomposition, phase change and thermal stability. This study proposes and develops a MEMS chip-based TG/DTA microsystem that integrates both programmed heating and detecting elements into a TG chip and a DTA chip to enable the microinstrument performing TG/DTA joint characterization under microscope observation. The TG chip contains a self-heating resonant microcantilever to measure heating-induced mass change of a sample and the DTA chip is with a microheater and a temperature-detecting thermopile integrated on a suspended thermal-insulating diaphragm. Only nanogram and microgram-level samples are needed for the TG and DTA chips, thereby achieving safe measurement to energetic materials such as strong oxidants. The chip-based microinstrument surpasses the state-of-the-art commercial TG/DTA instruments that have, in the long term, suffered from large sample-amount (milligram level. This point of intersection is very significant for several reasons including thermal stability indicator, characterization of phases such as indication of the transformation between phases such as transition between forms of NiO or related reactions that can affect chemical properties and prediction of the material's response or behaviour under operating conditions which is crucial for applications in catalysis, electronics and other high-temperature applications.

The DSC analysis (Fig. 12) confirms that the NiO sample undergoes two main thermal events within the tested temperature range: the evaporation of water at around 160 °C and the crystallization/grain growth of the nanoparticles starting around 200 °C and peaking around 250 °C. This result is consistent with the findings from the TGA analysis, which also showed a weight loss due to the removal of volatile components at a similar temperature range.

The endothermic peak observed for the synthesized nickel (II) oxide nanoparticles at 162 °C and –30 mW in the DSC curve typically indicates a well-defined phase

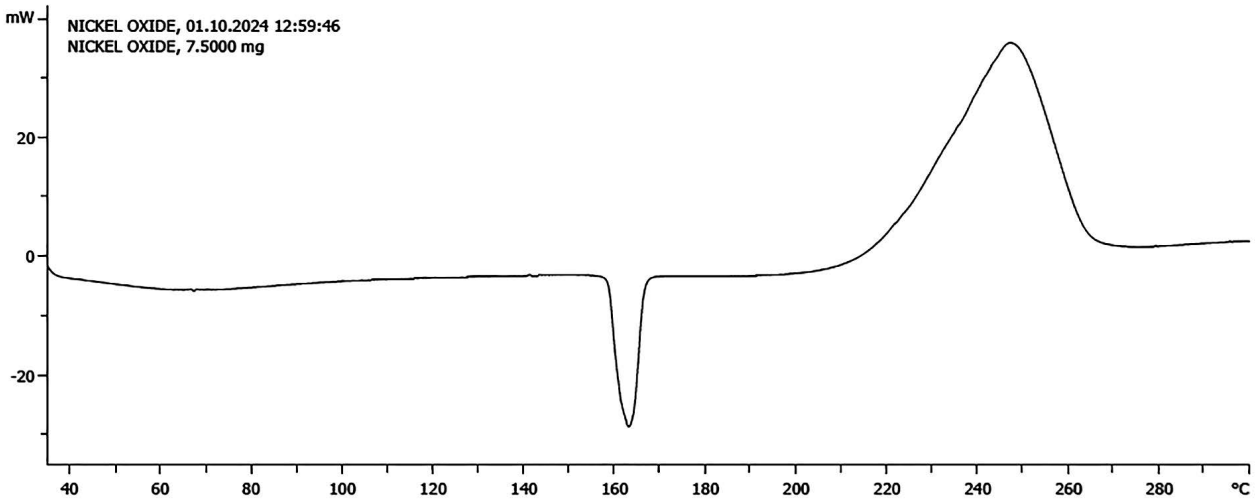

Fig. 12. DSC Analysis for the synthesized Nickel (II) oxide nanoparticles

transition or a specific thermal event such as melting or decomposition of a crystalline structure. In this case, the characteristic temperature of 162 °C suggests a significant change in the material's state or structure which could involve the melting of a phase or the rearrangement of the crystal lattice. The negative value indicated by –30mW signifies that the material is absorbing heat at this temperature implying an endothermic process.

This can be related to the breakdown of a stable form of nickel (II) oxide or the onset of a structural transformation. The strong endothermal peak at 162 °C suggests a critical point for the nickel (II) oxide nanoparticles possibly marking the start of instability or transformation in the material [55]. The exothermic peak at 250 °C reflects subsequent reactions or transformations that may be occurring as the temperature increases. The broad nature of the peak suggests that these processes involve a range of components or interactions such as particle coalescence, oxidation, or thermal rearrangements indicating changes in material properties. Together, these peaks provide valuable insights into the thermal stability and reactivity of nickel (II) oxide nanoparticles which is crucial for their applications in catalysis, electronics, energy storage and other applications.

Corrosion rate and inhibition efficiency

Figures 13 to 15 give a summary of the weight loss, corrosion rate and inhibition efficiency of uncoated and coated mild steel samples immersed in 3.5 wt. % NaCl for 60 days at room temperature.

The effects of the variation in the inhibitor concentration and exposure time had very significant influence on the metal weight loss. In general, Figure 13 reveals that increase in the inhibitor concentration resulted in a decrease in metal weight loss at room temperature which is an indication that the inhibitor

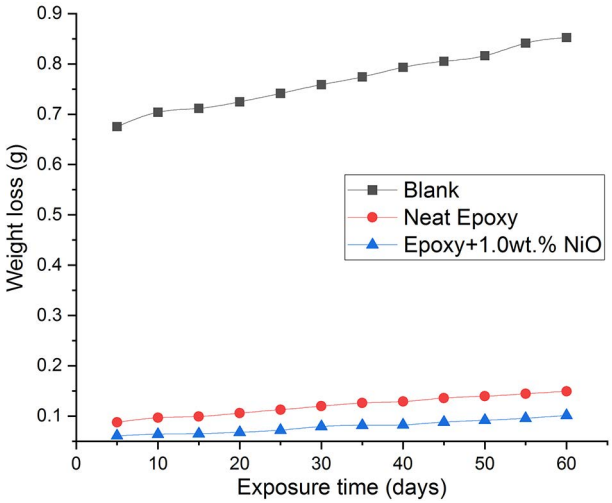

Fig. 13. Weight loss of uncoated and coated mild steel in 3.5 wt. % NaCl

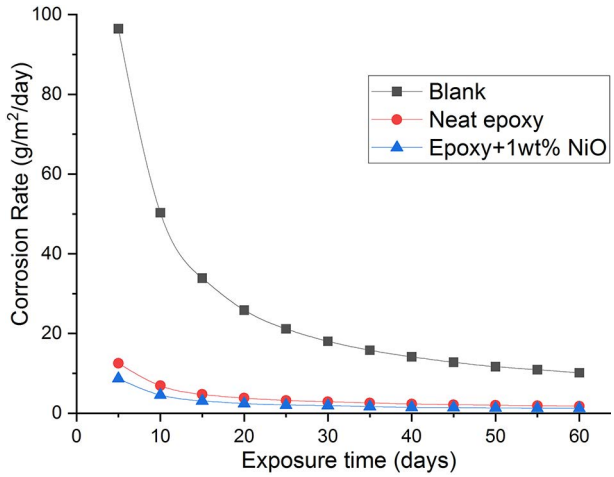

Fig. 14. Corrosion rate of uncoated and coated mild steel in 3.5 wt % NaCl

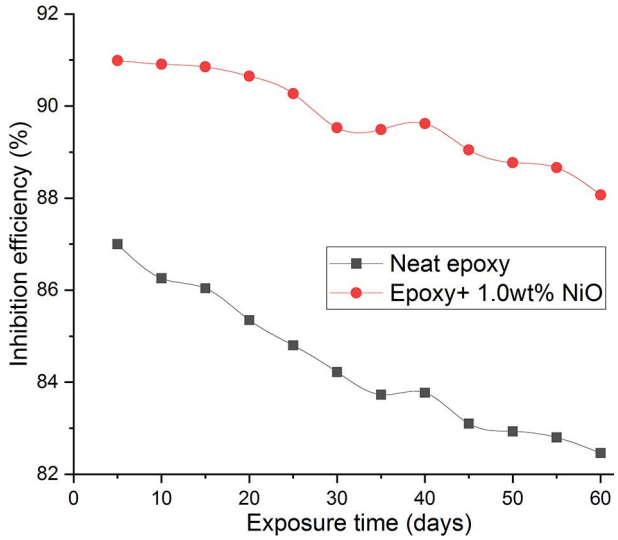

Fig. 15. Inhibition efficiency of uncoated and coated mild steel in 3.5 wt. % NaCl

retards the corrosion reaction process. The increase in weight loss of the metal with increase in the exposure time implies that corrosion is a continuous and time dependent process. The resistance to corrosion process exhibited by the epoxy-NiO nanocomposite can be explained in terms of the ability of the inhibitor to get adsorbed at the reaction sites (cathode and anode) on the metal surface by blocking the metal pores and forming a thin layer thereby preventing the free flow of electrons for corrosion reactions [56]**.** The corrosion resistance is also enhanced by the excellent barrier property of epoxy resin as well as the polar functional groups present in epoxy resin which serve as adsorption sites to the metal substrate [6]. The uncoated mild steel exhibited the highest corrosion rate of 96.47 g/m^2/day in 3.5 wt. % NaCl within the first five days of immersion due to surface exposure, immediate electrolyte contact leading a series of electrochemical reactions which initiate corrosion, formation of corrosion products, surface roughness, disruption of protective films and oxygen availability. The electrochemical reactions involve the anodic reaction i.e. oxidation of mild steel which is primarily composed of iron which leads to release of Fe^{2+} ions into the solution and cathodic reaction i.e. reduction reactions typically involving water and oxygen. The ions and hydroxides formed often lead to the creation of corrosion products which can accelerate further corrosion if they do not effectively passivate the surface. Upon immersion, any pre-existing surface oxide layer can be disrupted thereby exposing fresh metal to the electrolyte which increases the corrosion rate. The high concentration of ions in NaCl enhances conductivity, allowing for rapid electrochemical reactions [39]. Freshly exposed mild steel may have microstructural irregularities that can act as localized corrosion sites (anodic sites) heightening localized attack. The progressive reduction of corrosion rate from 96.47 g/m^2/day in 3.5 wt. % NaCl within the first five days to 10.15 g/m^2/day in 3.5 wt. % NaCl after 60 days of immersion can be attributed to passivation, depletion of reactive species, stabilization of corrosion products and inhibition by passive films. Over time, corrosion products may form a layer that can partially protect the mild steel surface, slowing corrosion rates. As the corrosion process continues, the concentration of reactive species may decrease, reducing the driving force for the electrochemical reaction. The formation of stable corrosion products can reduce the diffusion of ions to the metal surface. If less soluble corrosion products form, they can adhere to the steel surface, leading to the establishment of passive film behaviour. The relatively low corrosion rate of 12.54 g/m^2/day observed for the mild steel sample coated with only epoxy resin within the first five days of immersion in 3.5 wt. % NaCl can be attributed to the barrier properties of epoxy resin. The epoxy coating acts as a physical barrier, limiting direct contact of the salt solution with the underlying metal, drastically reducing initial corrosion rate. The mild steel sample coated with epoxy-1 wt. % NiO exhibited corrosion rate of 8.69 g/m^2/day within the same period of exposure which was lower than the corrosion rate observed for mild steel sample coated with only neat epoxy resin as well as the uncoated mild steel sample. This shows that nickel (II) oxide nanoparticles have imparted some electrochemical properties that can enhance the overall resistance to corrosion. Nanoparticles can also alter the charge distribution and surface characteristics, potentially inhibiting localized corrosion rates. It can be seen from figure 14 that the inhibition efficiency generally increases with an increase in the wt. % of NiO in the epoxy-nickel oxide nanocomposite coatings but decreases with prolonged exposure ti-me. This can be attributed to prolonged exposure to saline conditions, stress, moisture, mechanical wear, leaching of nanoparticles into the solution, loss of contact of nanoparticles with the substrate and possible delamination which can compromise the protective properties of the coatings. Maximum efficiency values of 87 % and 91 % were recorded for the neat epoxy coated sample and the MS sample coated with 1 wt. % NiO respectively.

Effect of temperature

The effect of temperature on the corrosion rate and corrosion inhibition efficiency of mild steel in 3.5 wt. % NaCl using epoxy-NiO nanocomposites is illustrated in Figures 16 and 17 respectively.

It is evident from figure 16 that the increase in temperature significantly increased the corrosion rates of the coated and uncoated samples. The effect of temperature on corrosion rate is governed by an Arrhenius type relationship [57] shown in equation 4:

$$CR = A \exp\left(-\frac{Ea}{RT}\right) \quad (4)$$

where CR is the corrosion rate, R is the universal gas constant, T is the absolute temperature and A is a pre-exponential factor.

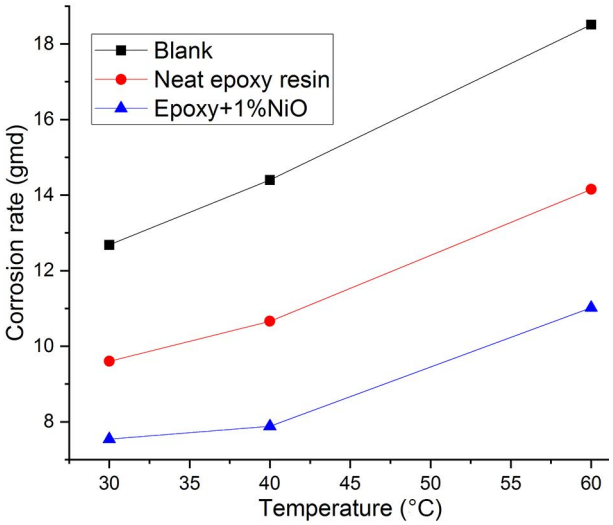

Fig. 16. Effect of temperature on corrosion rate

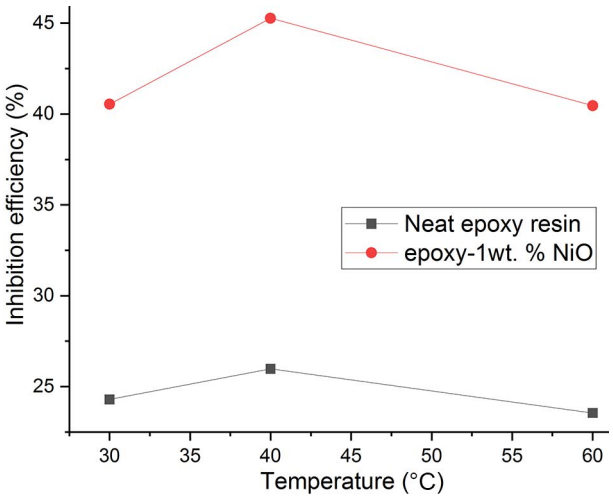

Fig. 17. Effect of temperature on inhibition efficiency

Computed values of activation energy, E_a from Arrhenius plots for the various samples were derived from the Arrhenius plots (Fig. 18) using the linear form of equation 7 and summarized in Table 2. The calculated values for activation energies were 10.62, 11.04 and 11.10 kJ/mol for the blank MS sample, neat epoxy coated MS sample and epoxy-1.0 wt. % coated MS samples respectively.

This trend indicates that less energy barrier is to be overcome in the blank sample for corrosion to take place compared to the neat epoxy resin coated sample and higher activation energy is required to initiate corrosion

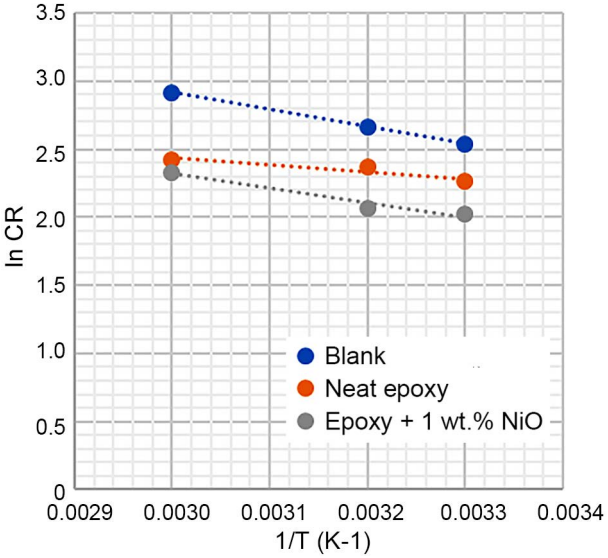

Fig. 18. Arrhenius plot for the various samples at 30-60 °C

Tab. 2 Computed activation energy values for the various samples

Sample description	Slope of graph (K)	E_a (kJ/mol)
Blank MS	–1 277.90	10.62
Epoxy coated MS	–1 327. 90	11.04
Epoxy-1% wt. % NiO coated MS	–1 336. 40	11.10

in samples protected by epoxy-NiO nanocomposite coatings. The decrease in inhibition efficiency of epoxy-NiO coatings at elevated temperatures can be attributed to a combination of factors and mechanisms including accelerated corrosion processes due to increased electrochemical activity; degradation of the coating structure, leading to microcracking, delamination, or loss of coating adhesion; increased permeability of the coating at higher temperatures, allowing chloride ions to penetrate and reach the mild steel substrate; alteration of the NiO particles‘ dispersion or surface interactions, which weakens their corrosion-inhibiting properties; thermal softening of the epoxy resin, increasing its susceptibility to ion penetration and decreasing the barrier properties [6], [39].

The epoxy coated mild steel samples immersed in 3.5 wt. % NaCl exhibited the least percentage inhibition efficiencies of 24.3 %, 26 % and 23.6 % at temperatures of 30 °C, 40 °C and 60 °C respectively while mild steel samples coated with epoxy- 1 wt. % NiO had the highest percentage inhibition efficiency values of 40.5 %, 45.3 % and 40.5 % at temperatures of 30 °C, 40 °C and 60 °C respectively and highest activation energy of 11.10 kJ/mol due to the enhanced corrosion resistance induced by the presence of nickel (II) oxide nanoparticles in epoxy resin.

Surface roughness analysis

The surface roughness values obtained from AFM characterization of the various samples after 60 days of immersion in 3.5 wt. % NaCl are presented in Table 3 while the AFM micrographs are illustrated in Figures 19 to 21.

The progressive reduction of surface roughness values from the blank with average value of 0.185 to the pure epoxy coated mild steel with average value of 0.121 and subsequently to the epoxy-NiO nanocomposite coatings containing 1.0 wt. % NiO with average values of 0.105 confirm that the corrosion rate is reduced as the concentration of NiO is increased in the epoxy resin. Lower surface roughness values generally indicate better protection against corrosion, as a smoother surface is less prone to localized corrosion or degradation which implies that lower surface roughness values generally enhance percentage inhibition efficiency. As NiO con-centration increases in the epoxy resin, the surface roughness decreases significantly which suggests that the NiO nanocomposites are contributing to a more uniform, smooth surface during immersion in 3.5 wt. % NaCl, indicative of better corrosion protection. The inhibition efficiency of 82.5 % after 60 days of immersion in 3.5 wt. % NaCl for pure epoxy resin coated MS sample increases when 1.0 wt. % NiO is added to the epoxy resin, reaching a peak of 88.1 % after 60 days of immersion in 3.5 wt. % NaCl. This is likely because the 1.0 wt. % NiO concentration provides a balance between optimal coating thickness, barrier properties, and smoothness (as seen in the relatively low surface roughness of 0.105 nm).

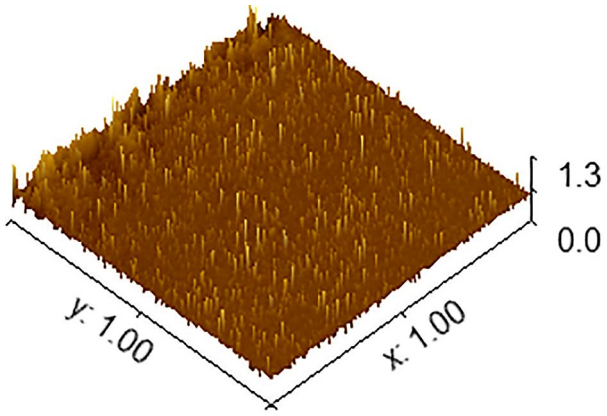

Fig. 19. 3-D AFM micrograph of blank sample in 3.5 wt.% NaCl

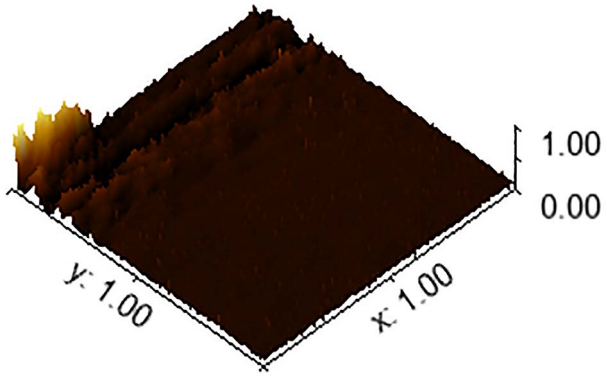

Fig. 20. 3-D AFM micrograph of epoxy resin coated sample in 3.5 wt.% NaCl

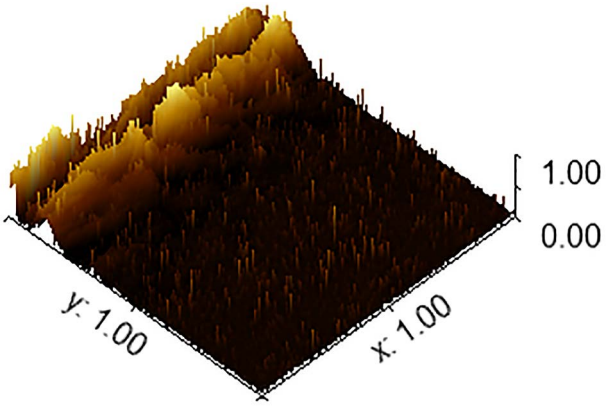

Fig. 21. 3-D AFM micrograph of epoxy-1.0 wt. % NiO coated Mild steel sample in 3.5 wt.% NaCl

CONCLUSION

The present study successfully demonstrates a novel, efficient, and scalable chemical precipitation route for synthesizing high-purity nickel (II) oxide (NiO) nanoparticles directly from dissolved nickel. Comprehensive characterization using XRD, FTIR, TEM, SEM-EDX, AFM, TGA/DTA, and DSC unequivocally confirmed the formation of thermally stable, crystalline NiO nanoparticles with a desirable average crystallite size of 23.03 nm with a narrow particle size distribution

Tab. 3 Surface roughness values of selected samples

Sample	Average value (nm)	RMS roughness (Sq) (nm)	RMS (grainwise) (nm)	Mean roughness (Sa) (nm)	Maximum peak height (Sp) (nm)	Maximum peak depth (Sv) (nm)
Blank	0.185	0.079	0.079	0.043	0.815	0.185
Epoxy coated MS	0.121	0.053	0.053	0.027	0.879	0.121
Epoxy-1wt% NiO coated MS	0.105	0.143	0.143	0.092	0.895	0.105

ranging from 10.02 to 28.50 nm. Furthermore, thermal analysis demonstrated the exceptional thermal stability of the material, a crucial property for its integration into high-performance polymer composites.

Beyond fundamental material insights, this research provides compelling evidence of the exceptional efficacy of these synthesized NiO nanoparticles as a corrosion inhibitor when incorporated into epoxy coatings for mild steel. The epoxy-NiO nanocomposite coating containing 1 wt. % NiO, exhibited a remarkable reduction in corrosion rate and significantly enhanced inhibition efficiency (up to 91.0 %) compared to pristine epoxy and uncoated mild steel, even under challenging saline conditions and elevated temperatures. This enhanced protection is attributed to the synergistic effect of the epoxy's barrier properties and the active inhibition mechanism facilitated by the well-dispersed NiO nanoparticles, which likely form a stable protective layer and hinder electrochemical reactions at the steel surface.

These findings establish a cost-effective and robust strategy for advanced metallic corrosion protection, offering a vital step towards prolonging the service life of steel structures in aggressive environments. The developed synthesis method and the demonstrated superior performance of the NiO nanocomposites hold immense promise for industrial applications in infrastructure, marine, and automotive sectors, where material degradation due to corrosion represents a significant economic and safety challenge. Future work will focus on further optimizing the nanoparticle morphology and concentration, investigating the long-term durability and self-healing capabilities of these coatings in diverse corrosive media, and exploring large-scale industrial implementation.

Declaration of Competing Interest

The authors declare that there are no conflicts of interest.

Acknowledgements

The authors are grateful to the Africa Centre of Excellence in Future Energies and Electrochemical Systems, Federal University of Technology, Owerri, Imo State, Nigeria and the World Bank for providing the facilities and enabling environment to carry out this work. The authors are immensely grateful to Mr. John Anyanwu and Miss Precious Okechukwu of the General-Purpose Laboratory of the Africa Centre of Excellence in Future Energies and Electrochemical Systems, Federal University of Technology, Owerri (ACE-FUELS, FUTO) for assisting with the AFM and FTIR characterization. The assistance of Engr. Abdulrahman Abdulhamid of Umaru Musa Yar'adua Central Research Laboratory, Katsina in carrying out the XRD, TGA/DTA and DSC characterization is highly appreciated. Mr. Akhihiero-Ata Samuel of the Department of Geology, University of Ibadan is also appreciated for assisting with the SEM-EDX and TEM characterization.

REFERENCES

1. Grilli, M. L. "Metal oxides," *Metals,* **2020**, 10 (6): p. 1–3, doi: 10.3390/met10060820.
2. Ren, B., Wang, Y. and Ou, J. Z. "Engineering two-dimensional metal oxides via surface functionalization for biological applications," *Mater. Chem. B*, **2020**, doi: 10.1039/C9TB02423A.
3. Mohammad, M. K., Syed, F. A. and Abdullah, A. "Metal oxides as photocatalysts," *J. Saudi Chem. Soc.*, **2015**, 19: p. 462–464, doi: 10.1016/j.jscs.2015.04.003.
4. Gouda, M. and Abd El-Lateef, H.M. "Novel cellulose derivatives containing metal (Cu, Fe, Ni) oxide nanoparticles as eco-friendly corrosion inhibitors for C-steel in acidic chloride solutions," *Molecules*, **2021**, 26 (22), doi: 10.3390/molecules26227006.
5. Anjum, M. J. et al. *Metal / metal oxide nanoparticles as corrosion inhibitors*. Elsevier Inc., **2020**, doi: 10.1016/B978-0-12-819359-4.00011-8.
6. Xavier, J. R. "Electrochemical, mechanical and adhesive properties of surface modified NiO-epoxy nanocomposite coatings on mild steel," *Mater. Sci. Eng. B*, **2020**, 260: p. 114639, doi: 10.1016/j.mseb.2020.114639.
7. Iqbal, A. et al. "Green synthesis of flower-shaped copper oxide and nickel oxide nanoparticles via capparis decidua leaf extract for synergic adsorption-photocatalytic degradation of pesticides," *Catalysts*, **2021**, 11 (7), doi: 10.3390/catal11070806.
8. Islam, R. et al. "Modulating Mn-doped NiO nanoparticles: structural, optical and electrical property tailoring for enhanced hole transport layers," *Nanoscale Adv.*, **2024**, doi: 10.1039/d4na00708e.
9. Barzinjy, A. A. et al. "Green and eco-friendly synthesis of Nickel oxide nanoparticles and its photocatalytic activity for methyl orange degradation," *J. Mater. Sci. Mater. Electron.*, **2020**, 31(14): p. 11303–11316, doi: 10.1007/s10854-020-03679-y.
10. Panigrahi, U.K. "Effect of Mg doping on the improvement of photoluminescence and magnetic properties of NiO nanoparticles," *Nano Express*, **2020**, 1 (2), doi: 10.1088/2632-959X/aba285.
11. Deshpande, M.P., et al. "Structural, thermal and optical properties of nickel oxide (NiO) nanoparticles synthesized by chemical precipitation method," *Adv. Mater. Res.*, **2016**, 1141: p. 65–71, doi: 10.4028/www.scientific.net/amr.1141.65.
12. Hadi, K. and Al- Saadi, T. M. "Investigating the structural and magnetic properties of nickel oxide nanoparticles prepared by precipitation method," *Ibn AL-Haitham J. Pure Appl. Sci.*, **2022**, 35 (4): p. 94–103, doi: 10.30526/35.4.2872.
13. Nakhaeenejad, S. et al. "Enhancing the efficiency of hole-transport-free perovskite solar cells using nickel oxide nanoparticles as a dopant in graphite-based carbon electrodes'', *J. Phys. Chem. Solids*, **2024**, 189: p. 111958, doi: 10.1016/j.jpcs.2024.111958.

14. Zhao, M. *et al.*, "Facile electrolysis-solvothermal synthesis of NiOx/graphene for enhanced ethanol oxidation to acetate," *Dalt. Trans.*, **2024**, 53 (9): p. 4237–4242, doi: 10.1039/d3dt03963c.
15. Dojer, B. and Kristl, J. "Synthesis of nickel and cobalt sulfide nanoparticles using a low cost sonochemical method," *Heliyon*, **2017**: p. 1–19, doi: 10.1016/j.heliyon.2017.e00273.
16. Fereshteh, Z. et al. "Synthesis of nickel oxide nanoparticles from thermal decomposition of a new precursor," *J. Clust. Sci.*, **2012**, 23 (2): p. 577–583, doi: 10.1007/s10876-012-0477-8.
17. Meher, S.K. Justin, P. and Rao, G. R. "Microwave-mediated synthesis for improved morphology and pseudocapacitance performance of nickel oxide," *ACS Appl. Mater. Interfaces*, **2011**, 3 (6): p. 2063–2073, doi: 10.1021/am200294k.
18. Shalichah, C. and Khumaeni, A. "Synthesis of nickel nanoparticles by pulse laser ablation method using Nd:YAG laser," *J. Phys. Conf. Ser.*, **2018**, 1025 (1), doi: 10.1088/1742-6596/1025/1/012002.
19. Olajire, A.A. and Mohammed, A.A. "Green synthesis of nickel oxide nanoparticles and studies of their photocatalytic activity in degradation of polyethylene films," *Adv. Powder Technol.*, **2020**, 31 (1): p. 211–218, doi: 10.1016/j.apt.2019.10.012.
20. Srihasam, K. et al. "Phytogenic generation of NiO nanoparticles using stevia leaf extract and evaluation of their in-vitro antioxidant and antimicrobial properties," *Biomolecules*, **2020**, 10 (1), doi: 10.3390/biom10010089.
21. Rifaya, M.N., Theivasanthi, T. and Alagar, M. "Chemical capping synthesis of nickel oxide nanoparticles and their characterizations studies," *Nanosci. Nanotechnol.*, **2012**, 2 (5): p. 134–138, doi: 10.5923/j.nn.20120205.01.
22. Salavati-niasari, M., Davar, F., and Fereshteh, Z."Synthesis of nickel and nickel oxide nanoparticles via heat-treatment of simple octanoate precursor," *J. Alloys Compd.*, **2010**, 494: p. 410–414, doi: 10.1016/j.jallcom.2010.01.063.
23. Danial, A.S. et al. "On the synthesis of nickel oxide nanoparticles by sol-gel technique and its electrocatalytic oxidation of glucose," *J. Power Sources*, **2018**, 293: p. 101–108, doi: 10.1016/j.jpowsour.2015.05.024.
24. Hada, R. et al. "A novel synthesis process for making nickel oxide nanoparticles," *Int. Res. J. Pure Appl. Chem.*, **2013**, 3 (2): p. 111–117.
25. Nathan, T., Aziz, A., Noor, A. F. and Prabaharan, S. R. S. "Nanostructured NiO for electrochemical capacitors: Synthesis and electrochemical properties," *J. Solid State Electrochem.*, **2008**, 12 (7): p. 1003–1009, doi: 10.1007/s10008-007-0465-3.
26. Ortega, D. et al. "Phase, size and shape controlled formation of aerosol generated nickel and nickel oxide nanoparticles," *J. Alloys Compd.*, **2013**, 579: p. 495–501, doi: 10.1016/j.jallcom.2013.06.128.
27. Sheit, H. M. K. et al. "Enhanced anti-corrosion efficiency and antimicrobial properties of green synthesised nickel oxide (NiO) nanoparticles," *Res. Sq.*, **2023**, p. 1–27.
28. Firisa, S. G., Muleta, G. C., and Yimer, A. A. "Synthesis of nickel oxide nanoparticles and copper-doped nickel oxide nanocomposites using *Phytolacca Dodecandra* l ' herit leaf extract and evaluation of its antioxidant and photocatalytic activities," *ACS Omega*, **2022**, 7: p. 44720–44732, doi: 10.1021/acsomega.2c04042.
29. Ndukwe, A. I. et al. "Metal corrosion in high temperature conditions: A review," *Zast. Mater.*, **2025**, 65: p. 1–25, doi: 10.62638/ZasMat1203.
30. Nwigwe, U. S., Umunakwe, R. and Okon, K. "The inhibition of *Carica Papaya* leaves extract on the corrosion of cold worked and annealed mild steel in HCl and NaOH solutions using a weight loss technique," *Eng. Appl. Sci. Res.*, **2019**, 46 (2): p. 114–119, 2019, doi: 10.14456/easr.2019.14.
31. Ndukwe, A.I., Ozoh, C. C. and Okon, K. "The inhibition of mild steel corrosion by papaya and neem extracts," *Mater. Prot.*, **2023**, 64 (3): p. 274–282, doi: 10.5937/zasmat2303274N.
32. Okon, K. et al. "Corrosion inhibition of mild steel and aluminium using extracts of vernonia amygdalina: A review," *Nexus Futur. Mater.*, **2025**, 2 (1): p. 154–166, doi: 10.70128/590516.
33. Okon, K., Ayogu, I. I., Azeez, T. O., and Akalezi, C. O. "Artificial neural network modelling of corrosion inhibition of mild steel in marine environment using epoxy-nickel oxide nanocomposite coatings," *World J. Mater. Sci. Technol.*, **2025**, 2 (1):p. 9–26, 2025, doi: https://doi.org/10.11648/j.wjmst.20250201.12.
34. Agu, P. C. *et al.*, "Response evaluation of mild steel corrosion rate in H_2SO_4 to the synegistic influenceof exposure time and steel weight loss," *J. Innov. Res. Eng. Sci.*, **2025**, 6 (1):p. 634–651, 2025, Online: available: https://journals.unizik.edu.ng/joires/about%0AResponse
35. Agu, P. C. *et al.*, "Multi-factorial prediction of mild steel exposure time during its corrosion inhibition with *Hibiscus Sabdariffa* leaf extract in 0.5 M H_2SO_4," *J. Innov. Res. Eng. Sci.*, **2025**, 6 (1): p. 652–665.
36. Okon, K. et al. "Recent advances in the use of metal oxides as corrosion inhibitors: a review," *KOM-Corrosion Mater. Prot. J.*, **2025**, 69: p. 14–33, doi: 10.2478/kom-2025-0003.
37. Okon, K. et al. "Recent progress in the application of nickel (nickel oxide nanoparticles) nanocomposites as corrosion inhibitors," *Port. Electrochim. Acta*, **2026**, 44 (4): p. 267–287, doi: https://doi.org/10.4152/pea.2026440402.
38. Okon, K. et al. "ANN Modelling of corrosion inhibition of mild steel in marine environment using epoxy-nickel oxide nanocomposite coatings," *Acad. J. Manuf. Eng.*, **2025**, 23 (2): p. 32–42, doi: 10.5281/zenodo.15863489.
39. Khodair, Z. T., Khadom, A. A., and Jasim, H. A. "Corrosion protection of mild steel in different aqueous media via epoxy/nanomaterial coating: preparation, characterization and mathematical views," *J. Mater. Res. Technol.*, **2018**: p. 1–12, doi: 10.1016/j.jmrt.2018.03.003.
40. Ali, A., Chiang, Y. W., and Santos, R. M. "X-ray diffraction techniques for mineral characterization: a review for engineers of the fundamentals, applications, and research directions," *Minerals*, **2022**, 12 (2), doi: 10.3390/min12020205.
41. Fatimah, S., Ragadhita, R., Al Husaeni, D. F., and Nandiyanto, A. B. D. "How to calculate crystallite size from x-ray diffraction (XRD) using Scherrer method," *ASEAN J. Sci. Eng.*, **2022**, 2 (1): p. 65–76, doi: 10.17509/ajse.v2i1.37647.
42. Dolabella, S., Borzì, A., Dommann, A. and Neels, A. "Lattice strain and defects analysis in nanostructured semiconductor materials and devices by high-resolution X-ray diffraction: theoretical and practical aspects," *Small Methods*, vol. 6, no. 2, **2022**, doi: 10.1002/smtd.202100932.

43. Cameron, F. H. and Raymond, E. S. "Tutorial on powder X-ray diff raction for characterizing nanoscale materials," *ACS Nano*, **2019**, doi: 10.1021/acsnano.9b05157.
44. Srivastava, P. C. and Srivastava, N. "Realizing NiO nanocrystals from a simple chemical method," *Bull. Mater. Sci.*, **2010**, 33: p. 653–656, doi: 10.1007/s12034-011-0142-0.
45. Mohammad, M., Irfan, A. and Mohd, S. "Investigation into the highly efficient *Artemisia Absinthium* – silver nanoparticles composite as a novel environmentally benign corrosion inhibitor for mild steel in 1M HCl," *J. Adhes. Sci. Technol.*, **2022**: p. 1–26, 2022, doi: 10.1080/01694243.2022.2075523.
46. Singh, A. *et al.*, "Structurally and morphologically engineered single-pot biogenic synthesis of NiO nanoparticles with enhanced photocatalytic and antimicrobial activities," *J. Clean. Prod.*, **2022**, 343, doi: 10.1016/j.jclepro.2022.131026.
47. Haq, S. *et al.*, "Antimicrobial and antioxidant properties of biosynthesized of NiO nanoparticles using R*aphanus Sativus* (R. sativus) extract," *Mater. Res. Express*, **2021**, 8 (5), doi: 10.1088/2053-1591/abfc7c.
48. Blanco, I. and Siracusa, V. "The use of thermal techniques in the characterization of bio-sourced polymers," *Materials (Basel).*, **2021**, 14 (7), doi: 10.3390/ma14071686.
49. Majder-Łopatka, M. *et al.*, "Thermal analysis of plastics used in the food industry," *Materials (Basel).*, **2022**, 15 (1), doi: 10.3390/ma15010248.
50. Asyraf, M. R. M. *et al.*, "Thermal properties of oil palm lignocellulosic fibre reinforced polymer composites: a comprehensive review on thermogravimetry analysis", **2023**, 30(5), *Springer Netherlands*, doi: 10.1007/s10570-023-05080-4.
51. Qaiss, K. "Graphene and nanoparticles hybrid nanocomposites from preparation to applications". *Composites Science and Technology*, **2021**, doi: 10.1007/978-981-33-4988-9.
52. Sai Revanth, J. et al. "TGA and DSC analysis of vinyl ester reinforced by Vetiveria zizanioides, jute and glass fiber," *Mater. Today Proc.*, **2019**, 26: p. 460–465, doi: 10.1016/j.matpr.2019.12.082.
53. Nurazzi, N. M. *et al.*, "Thermogravimetric analysis properties of cellulosic natural fiber polymer composites: A review on influence of chemical treatments," *Polymers (Basel).*, **2021**, 13 (16), doi: 10.3390/polym13162710.
54. Zhou, W. *et al.*, "Chip-based mems platform for thermogravimetric/differential thermal analysis (tg/dta) joint characterization of materials," *Micromachines*, **2022**, 13 (3): p. 1–11, doi: 10.3390/mi13030445.
55. Simonenko, T. L. et al. "Hydrothermal synthesis of a cellular NiO film on carbon paper as a promising way to obtain a hierarchically organized electrode for a flexible supercapacitor," *Materials (Basel).*, **2023**, 16 (15), doi: 10.3390/ma16155208.
56. Ibrahim, M. et al. "Enhanced corrosion protection of epoxy/ZnO-NiO nanocomposite coatings on steel," *Coatings*, **2020**, 10 (783): p. 1–14, doi:10.3390/coatings10080783.
57. Ndukwe, A. I. and Anyakwo, C. N. "Corrosion inhibition model for mild steel in sulphuric acid by crushed leaves of *Clerodendrum Splendens* (Verbenaceae)," *Int. J. Sci. Eng. Appl. Sci.*, **2017**, 3 (3): p. 39–49.